

# Lasing in quasi-periodic and aperiodic plasmon lattices

A. HINKE SCHOKKER AND A. FEMIUS KOENDERINK\*

Center for Nanophotonics, FOM Institute AMOLF, Science Park 104, 1098 XG Amsterdam, The Netherlands

\*Corresponding author: f.koenderink@amolf.nl

Received 11 April 2016; revised 27 May 2016; accepted 27 May 2016 (Doc. ID 262946); published 23 June 2016

**Plasmonic particle arrays enable unconventional miniature lasers by virtue of feedback by enhanced scattering, field confinement, and diffractive resonances. Here, we demonstrate lasing in quasi-periodic and aperiodic Galois, Thue–Morse, Fibonacci, paperfolding, Rudin–Shapiro, and randomized lattice arrangements of silver particles spanning the Fourier spectrum from discrete (period-like) to increasingly continuous (random-like). Through high-NA back-focal plane images we find that the laser output displays the rich Fourier spectrum of the lattice. Conversely, the real-space output at the laser plane is similar to speckle, yet with distinctly structured autocorrelations. Further, we identify many new lasing conditions on the basis of pseudo-Bragg conditions that do not occur for periodic arrays. This work enables controlled studies of lasing for any level of spatial correlation in the feedback mechanism going from periodic to random and shows that metasurface lasers offer new beam-shaping strategies.** © 2016 Optical Society of America

**OCIS codes:** (250.5403) Plasmonics; (140.3490) Lasers, distributed-feedback; (050.1940) Diffraction.

<http://dx.doi.org/10.1364/OPTICA.3.000686>

## 1. INTRODUCTION

Enhancing light–matter interactions is a much-studied subject that has both scientific and technological interest for fields ranging from enhancing spectroscopy [1], lighting applications [2], sensors [3,4], and photovoltaic structures [5,6] to quantum optics [7]. Plasmonics is a promising route to enhance light–matter interactions based on the strong coupling of light to resonant electron density oscillations in noble metals [8]. Metal particles exhibit strong scattering and tight near-field light confinement. Moreover, when plasmonic nanoparticles are placed in periodic arrays, even stronger interactions can occur due to the coupling of individual particle resonances to the diffraction modes of the lattice, creating sharp and low-loss lattice resonances that are particularly attractive for sensing, directional solid-state lighting, and surface-enhanced Raman scattering [9–11]. This type of diffractive plasmon resonance has recently been employed by several authors to realize plasmonic distributed feedback (DFB) lasers [12–17]. The large scattering strength per plasmonic particle gives rise to strong feedback, much stronger than in conventional dielectric DFB lasers, which typically utilize small index-contrast periodic gratings. Complementary to DFB lasing that relies on feedback by periodicity, lasing can also arise in completely random arrangements of dielectric scatterers that cause strong multiple scattering and are embedded in a gain medium [18–21]. In contrast to DFB lasing, a “random laser” results in non-directional and multifrequency laser emission.

In this paper, we study plasmon lasers intermediate to periodic and random systems, consisting of aperiodic arrays [22–31]. Aperiodic arrays are generated according to a deterministic generation sequence,

are not translationally invariant, and yet, can have strong spatial correlations [32]. Although quasi/aperiodicity was introduced as a purely mathematical discovery, a link was made with physics when it was shown that certain metallic alloys have a quasi-periodic ordering [33]. Quasi-periodicity has since then become hugely important in crystallography, as recognized by the 2011 Nobel Prize in Chemistry awarded to Shechtman. In optics, the photonic properties of aperiodic arrays have been the subjects of study, especially in the framework of one-dimensional (1D) and two-dimensional (2D) photonic crystals and in the case of plasmonics focused on 2D particle lattices [26,30,34,35]. In the context of plasmonics, there are two main reasons for which aperiodic systems have received interest. First, numerical studies [36] have claimed that aperiodic plasmonic particle arrays give rise to large local-field enhancements. Second, as opposed to periodic arrays, aperiodic systems exhibit a broadband optical response [23]. These properties could make aperiodic systems applicable in many areas, such as biosensors and engineered SERS substrates [27,37,38]. In LEDs, quasi-periodicity was shown to result in efficient light extraction, competitive with diffractive outcoupling but over larger bandwidths [39]. On a fundamental level, particular aperiodic arrays are believed to give rise to *critically localized* modes that are characterized by multifractal spatial patterns, large fluctuations of the local density of states, and high near-field enhancement [40]. These modes are distinct from the infinitely spatially extended Bloch modes of periodic systems and the exponentially localized modes of random media (assuming Anderson localization is achieved [41]).

Studies on lasing action in aperiodic systems so far all considered dielectric systems, such as quasi-periodic photonic crystal

lasers [42–45]. To our knowledge, these all relied on high-index dielectric structures with aperiodic arrangements of weakly scattering air holes. In this paper, we study aperiodic lasers consisting of strongly scattering plasmonic particles. The rationale is that plasmon particles have very large per-particle scattering cross sections compared to their dielectric counterparts. This enables the systematic study of lasing in deterministic aperiodic systems. In this work, we study lasing in a suite of systems that spans the entire scale from periodic to randomized, as gauged by their Fourier transform. We find lasing across the entire spectrum, from structures with infinitely sharp Fourier transforms (pure-point spectrum, as occurs for periodic and quasi-periodic systems) to structures with absolutely continuous Fourier transforms, similar to random systems [29]. We study laser output in terms of spectra, thresholds, k-space radiation patterns, and real-space speckle properties.

## 2. APERIODIC PLASMONIC LATTICE STRUCTURES

We fabricate arrays of silver disks on glass coverslips using electron beam lithography, thermal evaporation, and lift off, following the procedure described in Ref. [16]. The silver particles have a diameter of 100 nm and a height of 30 nm. We use a thin chromium adhesion layer. We create the aperiodic lattices from a square grid by removing particles according to given generation sequences for the Galois, Thue–Morse, Fibonacci, paperfolding, and Rudin–Shapiro lattices [29]. After fabricating the particle arrays, we spin-coat a 450 nm-thick layer of SU8 that acts as the gain medium by virtue of doping with Rhodamine 6G (Rh6G). This is achieved by mixing 5.25 mg of Rh6G with 1 ml of cyclopentanone (the solvent of SU8) and adding that to 1 ml of Microchem SU8-2005. Sonication for 10 minutes promotes mixing. The resulting solution is spincoated at 3000 rpm. The resulting dye density in solid SU8 is about 0.4 wt%, or 40 mM. The layer not only acts as gain medium but, owing to its index of 1.6 (from ellipsometry), it acts as a waveguide that supports one TE and one TM mode and provides good field confinement in the gain medium. These choices of material, doping, and thickness are identical to those in recent work on periodic plasmon lattice lasers [16,46]. Full-wave scattering calculations [16] show that the particle resonance in the glass/SU8/air system occurs at around 670 nm. We fabricated samples with three underlying pitches, namely  $d = 380, 300,$  and 190 nm (particles are smaller to avoid touching). Bragg’s law predicts a diffraction condition whenever  $d = m\lambda_{WG}/2$ , with  $\lambda_{WG} = \lambda_0/n_{WG}$  as the effective waveguide mode wavelength at mode index  $n_{WG} = 1.55$ . For a particle pitch of 380 (190) nm, the second- (first-) order Bragg diffraction condition for the TE mode occurs within the bandwidth of the fluorescence of the dye, whereas for a pitch of 300 nm, neither falls in the gain window. The gain window is on the blue flank of the dipolar plasmon resonance, where particle extinction cross sections are of the order  $0.04 \mu\text{m}^2$ . To illustrate the array generation procedure, as an example, we discuss the Fibonacci sequence. For this sequence, the  $n$ th generation is obtained by concatenating generations  $n - 2$  and  $n - 1$ , so that from start values A, B one obtains the sequence A, B, AB, BAB, ABBAB, BABABBAB, ABBABBABABBAB, etc. We identify  $A(B)$  with the absence (presence) of a particle. To extend the 1D grating to a 2D particle array, several methods exist [47]. Following Ref. [40], for each lattice site  $m$  in the 1D particle row, we transpose the row to define a column vector. This directly

defines the  $m$ th column of the 2D lattice whenever the  $m$ th entry in the 1D grating is occupied. Whenever the  $m$ th site, however, is empty, the  $m$ th column is obtained by flipping all entries. This extension algorithm is used for all deterministic lattices, starting from their known 1D recursions. The random sample is defined by removing 50% of the particles randomly from the square grid, thereby having exactly the same fill factor and underlying square grid correlation as all the aperiodic systems. We note that recent work [46] showed that such randomized square lattice lasers are remarkably robust to removing and shuffling particles, as these are disordering mechanisms that retain long-range correlations. This should be contrasted to other randomization methods [48–50].

Figures 1(a)–1(g) show scanning electron microscope (SEM) images of the various lattices we fabricated (sample pitch 380 nm), while Figs. 1(h)–1(n) shows Fourier transforms (absolute value of discrete Fourier transform (DFT), or “structure factors”) for all lattices. These Fourier transforms are not obtained from SEM images, but rather, from finite truncations (250 periods across, similar to the size of the experimentally studied fields) of the mathematically generated lattices, where Gaussian apodization reduces truncation artifacts. For the periodic lattice, the DFT necessarily corresponds to the reciprocal lattice, i.e., isolated  $\delta$ -spikes in a square grid of spacing  $2\pi/d$ . For the Galois, Thue–Morse, and Fibonacci lattices, many additional features appear as consequence of quasi/aperiodicity. In the random system, while the Brillouin zone is essentially uniformly filled, the diffraction features at  $2\pi/d$  still stand out. This is due to the fact that randomization by particle removal from a random lattice still leaves spatial correlations [46].

We organize the results in this paper according to a mathematical measure called “spectral flatness”, or Wiener entropy, introduced for this purpose by [24]

$$\text{SF} = \frac{\sqrt{\prod_{n,m}^{N,M} |\text{DFT}\{s(n, m)\}|}}{\frac{1}{NM} \sum_{n,m}^{N,M} |\text{DFT}\{s(n, m)\}|}. \quad (1)$$

Input for this quantity is the digitized structure, essentially a matrix of 0’s and 1’s representing the absence and presence of particles in a site  $(m, n)$ . The denominator is the geometric mean of the discrete Fourier transform  $\text{DFT}\{s(n, m)\}$  of the digitized structure, while the numerator represents the arithmetic mean. For infinite periodic structures (pure point spectrum), the spectral flatness equals 0, while for a random structure (absolutely continuous Fourier spectrum), the spectral flatness tends to 1. Table 1 lists the spectral flatness calculated numerically from the DFTs of truncated digital arrays, showing an increase from low to high values as the lattices vary from periodic to random. Note that neither the extremum 0 nor 1 is obtained for the periodic or random lattice. We attribute this to the apodization in real space and the correspondingly chosen finite discretization in the k-space sampling of the DFTs. Also, it is well known that for some structures, the convergence of spectral flatness with structure truncation is slow. As our experiments are conducted on finite structure areas, we choose to present values appropriate for the experimentally truncated samples. Finally, while spectral flatness is one ordering metric, it is not a unique measure. In terms of the nature of the k-space spectrum, the periodic, Galois, Fibonacci, and paperfolding structures are known to have a discrete, or “pure-point” spectrum [29], while the Thue–Morse structure presents a singular

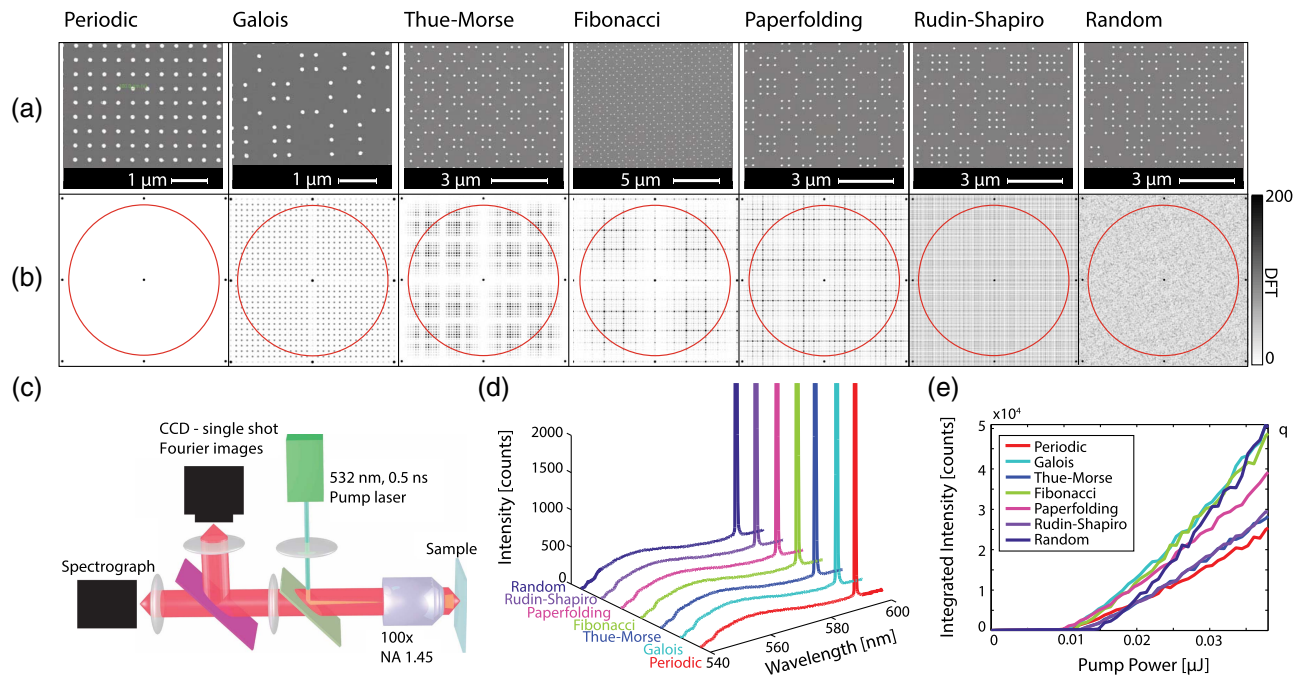


**Fig. 1.** Panel (a): SEM images of the arrays for a particle pitch of 380 nm; underneath it, the discrete Fourier transform of the corresponding array (Panel b). Red circles indicate the wave vector range available to a  $NA = 1.45$  objective, assuming a 380 nm pitch and 590 nm emission wavelength. Panel (c) shows a set-up diagram indicating Fourier imaging. Panel (d) shows spectra above the lasing threshold for periodic, Galois, Thue–Morse, Fibonacci, paperfolding, Rudin–Shapiro, and random arrays. The lasing wavelength is the same to within 1 nm for all arrays and corresponds to the wavelength for which the second-order Bragg diffraction condition holds for a pitch of 380 nm. Input–output curves are shown for all arrays in panel (e). From these curves, we obtain threshold pump powers of 12.5, 13.5, 15.6, 14.6, 12.5, 15.6, and 18.7 nJ.

**Table 1. Calculated Spectral Flatness (SF) and Measured Threshold Pump Power  $P_{th}$  Required to Obtain Lasing for Pitch 380 nm. Also Reported Is Whether the k-Space Spectrum of the Structure is Pure-Point (PP), Singular Continuous (SC), or Absolutely Continuous (AC)**

Structure	SF	$P_{th}$ [nJ]	Spectrum
Periodic	0.005	12.5	PP
Galois	0.04	13.5	PP
Thue–Morse	0.13	15.6	SC
Fibonacci	0.17	14.6	PP
Paperfolding	0.35	12.5	PP
Rudin–Shapiro	0.81	15.6	AC
Random	0.84	18.7	AC

continuous spectrum, and the Rudin–Shapiro sequence is pseudo-random (absolutely continuous). This distinction is clearly visible in the DFTs, where the Rudin–Shapiro lattice has a densely filled Brillouin zone with high spectral flatness, while the Thue–Morse structure has low spectral flatness, yet clearly a continuous part to its Fourier transform.

### 3. LASING OF APERIODIC SYSTEMS

We use an inverted fluorescence microscope in which the sample is excited from the glass side with a green (532 nm) laser that provides sub-nanosecond pulses in the sub-μJ range. Figure 1(c) shows a sketch of the inverted fluorescence microscopy imaging setup. We pump a spot of about 50 μm across and collect emission from the same side with an  $NA = 1.45$  objective, either on a

Andor CLARA CCD or with a Shamrock 303i spectrometer coupled to an Si CCD detector (Andor iVAC, <0.1 nm, resolution). For a sequence of 50 pump powers, we collect single-shot spectra, Fourier space images, and real-space images. The Fourier images are obtained by flipping an extra lens into the optical path at a focal distance away from the back focal plane of the imaging objective, in between the dichroic mirror and the tube lens of the CCD.

Figure 1(d) reports emission spectra above the lasing threshold for the seven structures, all at an underlying pitch of 380 nm. These spectra have been taken with the pump energy just a few percent above the lasing threshold and therefore show both the characteristic broad spontaneous emission spectrum of Rh6G, peaking around 550 nm, and a single sharp lasing line. All arrays have a lasing wavelength of approximately 591 nm corresponding to the second-order Bragg diffraction condition for the waveguide mode in the high-index slab at the underlying pitch of 380 nm. This result is consistent with our earlier study in which we randomly removed particles to obtain site occupation numbers as low as 1%, which all showed that the original periodic-lattice lasing condition is robust against particle removal [46]. Physically, this can be understood by noting that the Fourier transform in all cases shows strong peaks at the original reciprocal lattice vectors. Input–output curves for all arrays in Fig. 1 are obtained by plotting the emission intensity integrated over a bandwidth of 0.34 nm around the lasing peak. The input–output curves demonstrate a clear lasing threshold. Thresholds (see Table 1) vary by about a factor of 1.5, while slope efficiencies vary by about a factor of two. We note that thresholds would be hard to compare for lattices of different fill factors, and, unless they are on the same

sample substrate, due to variations in fabricating the waveguide. We emphasize that all lattices (except the periodic one) have an identical fill factor of 50%, and that the comparison is for an experiment run with all structures arrayed nearby on the same sample substrate. While threshold variations are hardly significant within the typical variation of 10% between nominally identical runs, the lowest thresholds are obtained in the structures with a “pure-point” low-spectral flatness Fourier transform. The more “random” structures, i.e., those with spectral flatness approaching the random system, tend to have a somewhat higher threshold. We further note that the large difference in slope efficiency between the periodic and quasi-periodic systems indicates that removing particles aids the outcoupling of the emission.

#### 4. LASING OUTPUT IN FOURIER SPACE

In terms of spectra and input–output curves, the quasi/aperiodicity appears to have no, or only a weak, effect on lasing. However, Fourier images, i.e., back-focal plane images, of the laser output clearly reflect the quasi/aperiodicity, as can be seen in Fig. 2. The images represent the output intensity as a function of the parallel emission wave vector  $\mathbf{k}_{\parallel} = \omega/c(\cos \phi, \sin \phi) \sin \theta$ , where  $\theta$  corresponds to the polar angle [angle with the optical axis], and  $\phi$  to azimuthal angle [16,51]. Thus, the center of each image corresponds to the optical axis, and the outer rim to the microscope NA (1.45), equivalent to about  $\theta = 72^\circ$  in glass. The Fourier image of the periodic lattice Fig. 2(a) shows a single peak in the center, which indicates lasing at the second-order Bragg condition. Dimly visible is furthermore a structure of eight intersecting circles, with a radius of curvature of 1.54. These correspond to the isofrequency contours of the waveguide dispersion (mode index of 1.54), repeated every reciprocal lattice vector, and are also seen in below-threshold fluorescence [16].

All a/quasi-periodic structures show additional structures. The structures range from discrete peaks that are comparable in intensity to the  $\mathbf{k}_{\parallel} = 0$  peak for the quasi-periodic lattices, [Figs. 2(a)–2(e) periodic, Galois, Fibonacci, and paperfolding] to a smoother (but speckled) background for the Thue–Morse, Rudin–Shapiro, and randomized cases [Figs. 2(c)–2(g)]. In

comparison, the below-threshold emission shows only a smooth, non-distinct angular dependence, punctuated with four rather indistinct circles of radius  $n_{\text{WG}} = 1.54$  (the TE-mode index) centered at reciprocal lattice vectors located at  $\lambda/d(\pm 1, 0)$  and  $\lambda/d(0, \pm 1)$  that reveal the repeated-zone-scheme waveguide dispersion relation [16].

Comparing the Fourier images in Fig. 2 with the Fourier transforms in Fig. 1 shows that the angular distribution of the laser output directly replicates the Fourier transform of the lattice. Therefore, whereas the lasing condition is unchanged when varying the periodicity from periodic to aperiodic, the outcoupling of the lasing mode is altered distinctly by the lattice. While the images in Fig. 2 are raw, single-shot images that suffer from saturation, we can also analyze this claim in more quantitative detail. To that end, for each lattice, we form a “high dynamic range (HDR)” dataset by combining the sequence of ten images in the pump power sweep just above the threshold. Our HDR algorithm sums images, except that as soon as the pixel values in the sequence are saturated, they are replaced by non-saturated values taken from the lower pump-power data, scaled for the power level. Next, we normalize the images to the Fourier image of just fluorescence in the absence of any lattice. Figure 3 shows a region of this data, normalized to the lasing peak at  $\mathbf{k}_{\parallel} = 0$ , alongside the absolute value of the structure factor (defined here as the absolute value of the discrete Fourier transform of the lattice). Since both the pitch and the lasing wavelength are known, this comparison does not require the scaling of the in-plane axes (wave vector calibration is known) or of the vertical axis. Excellent quantitative agreement is found, both for the *location* in wave vector space of salient peaks, and for relative intensities. This is further brought out by examining the cross cuts in Figs. 3(e)–3(h) averaged sideways to the cross cut over  $\Delta k = 0.02k_0$  along salient lines ( $k_{\parallel}/k_0 = [0.207, 0.524, 0.60, 0.391]$  for the Galois, Thue–Morse, paperfolding, and Fibonacci cases) in wave vector space. We conclude that also *quantitatively*, the lasing output in wave vector space corresponds to the Fourier transform of the lattice.

The fact that the lasing output simply represents the lattice Fourier transform is associated to a simple physical picture.

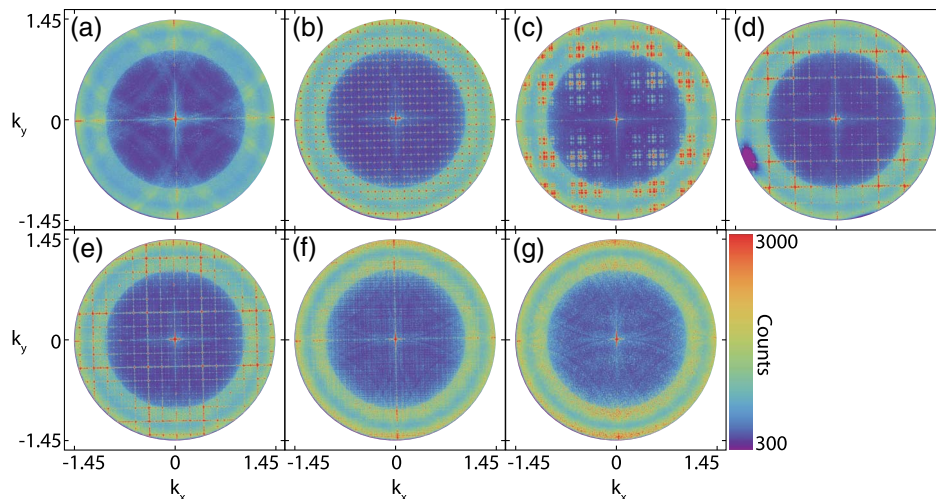


**Fig. 2.** Fourier images well above threshold for (a) periodic, (b) Galois, (c) Thue–Morse, (d) Fibonacci, (e) paperfolding, (f) Rudin–Shapiro (f), and random array (g). The Fourier images are obtained for an excitation energy of 0.05  $\mu\text{J}$ . For all quasi-periodic structures, extra peaks appear beside the second-order Bragg peak in the middle at  $\mathbf{k}_{\parallel} = 0$ . These coincide with maxima in the Fourier transform of the structure. It should be noted that these single-shot images well above the threshold are saturated in their bright pixels.

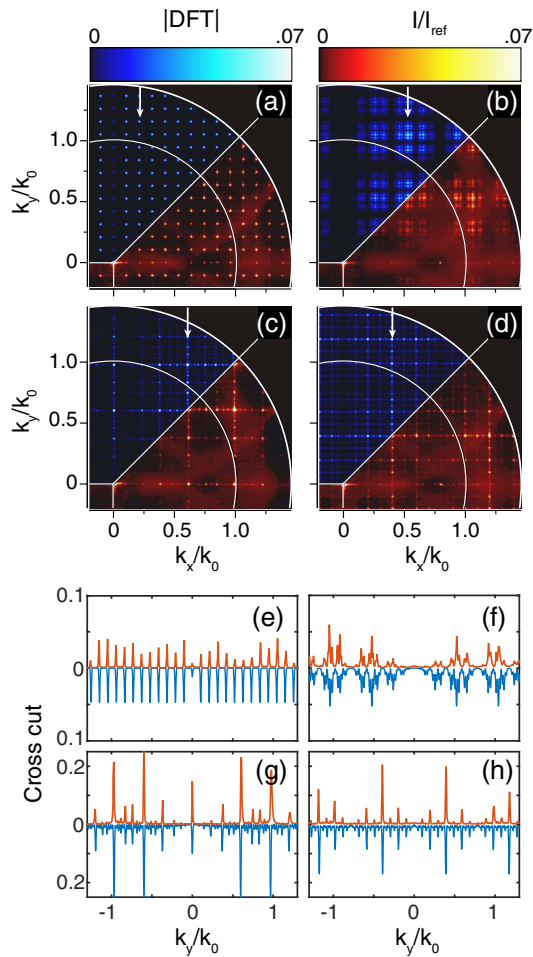


**Fig. 3.** Panels (a)–(d): Direct comparison of high dynamic range Fourier images of lasing in the Galois, Thue–Morse, paperfolding, and Fibonacci structures to the structure factors (DFTs). East-southeast quadrants (red): measured. Northern quadrants (blue): structure DFT (data and DFT normalized to the  $\mathbf{k} = 0$  peak, linear color scale). White circles: NA = 1 and 1.45 boundaries. White arrows:  $k_x/k_0$  values at which salient line traces along  $k_y$  are taken for panels (e)–(h). In each panel, the top (red) traces are data, while the downward (blue) traces are theoretical.

Essentially, the underlying laser mode is the same in all lattices, and carries wave vector  $\mathbf{k}_{\parallel} = 0$ , plus all diffraction orders  $\mathbf{k}_{\parallel} + \mathbf{G}$  of the original lattice. Upon outcoupling, the  $\mathbf{k}_{\parallel} = 0$  wave inherits the structure factor of the lattice as wave vector distribution. Indeed, according to phased array theory, the radiation pattern of a set of dipoles arranged in a plane and excited in phase exactly equals the Fourier transform of their spatial distribution. Thus, the lasing output has exactly the same wave vector structure as a diffraction pattern that one would obtain upon normal incidence excitation from the far field. Extrapolating this result, we propose that by deterministically removing particles from the original diffractive array, it is possible to retain the lasing output yet control its k-space distribution. This distribution is simply inherited from the Fourier transform of the binary amplitude mask that one can imprint at will by removing particles. This idea might even extend to phase masks that one could generate by changing the particle sizes in the vein of phase-gradient metasurfaces [52].

### 5. REAL-SPACE OUTPUT

In addition to Fourier space images, we also acquire real-space images of the sample plane, above and below the threshold. The below-threshold real-space images show plain Poissonian noise [46]. Above the threshold, patterns with large intensity fluctuations appear, which for random systems are known as speckle [53] and directly evidence spatial coherence. Examples are shown in Fig. 4 for all lattices. While for the randomized lattice, the laser’s speckle has all the properties expected of random-system speckle in terms of intensity statistics and autocorrelation [46], clearly the speckle from the deterministic aperiodic systems is structured in a manner reflecting the lattice in a non-trivial way. When taking an autocorrelation of these real-space images, this structure becomes evident. In particular, the quasi-periodic lattices show long-range correlations, while instead, the patterns with lower spectral flatness show a narrow autocorrelation of diffraction-limited widths. We note that the speckle patterns, even if seemingly random, in fact can be used for applications due to their autocorrelation function. For instance, large improvements to microscopy have recently been shown on the basis of using speckle [54–56]. Speckle provides a form of structured illumination microscopy where information is retrievable through the speckle autocorrelation that acts as point-spread function. From our work, it appears that deterministic aperiodic plasmon array

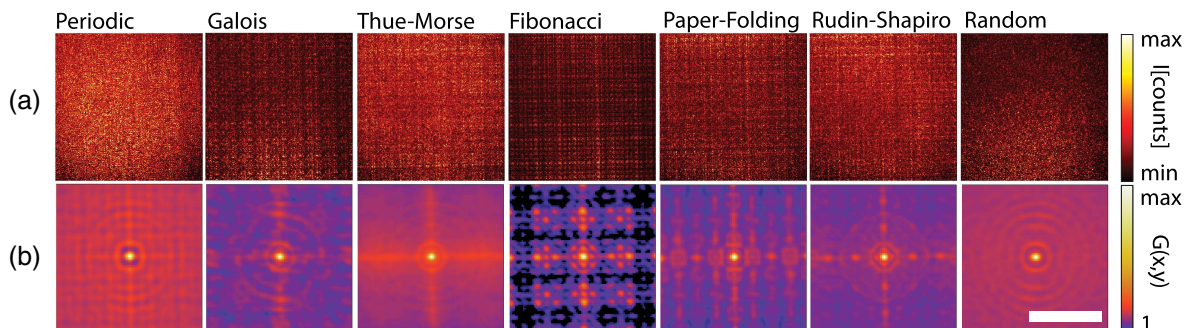


**Fig. 4.** Real-space images (a) and normalized autocorrelation (b) well above the threshold. The real-space images have 20  $\mu\text{m}$  field of view, and a clipped colorscale [ranges always corresponding to 1.4 times the minimum number of counts to 0.6 times the maximum number of counts]. Color ranges for autocorrelations are from 1.0 (minimum, no excess correlation) to the maximum correlation  $a$  at  $(x, y) = (0, 0)$ , which is 1.05, 1.12, 1.07, 1.14, 1.09, 1.07, resp. 1.1. This value mainly measures how far above threshold data was taken [46]. The scalebar is 3  $\mu\text{m}$  in all panels in (b).

lasers produce speckle patterns with controlled autocorrelations. In essence, this gives control over the point-spread function of speckle-based imaging techniques, similar to point-spread function control in raster-scanning imaging [57] or the use of gratings in structured illumination microscopy [58,59].

## 6. LASING AT OTHER DIFFRACTION CONDITIONS

Periodic systems only support extended Bloch states and only lase at Bragg conditions. Quasi-periodic systems, in contrast, may support many pseudo-Bragg conditions, and hence lase at different  $d/\lambda$  ratios [29]. Figure 5 shows spectra and Fourier images at maximum excitation power for arrays with a pitch of 300 nm. The periodic array does not show any lasing, as neither the first nor second Bragg diffraction condition for feedback is met in the gain window. The absence of lasing is verified not only by the lack of spectral feature, but also, we found no sign of lasing in the Fourier images (in which narrow angular features or speckle would emerge) or in the intensity fluctuations and correlations in the real-space sample images (which are sensitive to lasing even in strongly multi-modal cases [46]). For the other lattices, we do see lasing at various wavelengths. In particular, for the quasi-periodic lattices (Figs. 5(b), 5(d), and 5(e), the Galois, Fibonacci and paperfolding cases, respectively), we find discrete and reproducible lasing lines at low thresholds. For the lattices with large spectral flatness (the Thue–Morse [Fig. 5(c)], Rudin–Shapiro [Fig. 5(f)], and the random [Fig. 5(g)] lattices), we have to pump significantly harder (0.192  $\mu\text{J}$  for Rudin–Shapiro and 0.289  $\mu\text{J}$  for the random array, compared to 0.042  $\mu\text{J}$  for the Fibonacci structure) to then obtain lasing peaks more reminiscent of random lasing. Indeed, in Fig. 5, the quasi-periodic cases show isolated sharp peaks much like the  $d = 380$  nm case. In contrast, the Rudin–Shapiro and randomized lattice show an amplified

spontaneous emission peak near the gain maximum (550 nm), on top of which many narrow lasing peaks occur similar to those that random lasers show [19].

The Fourier images at the maximum excitation power in Fig. 5 for the periodic lattice show as the only visible features four circles, indicating that incoherent emission occurs preferentially in the waveguide mode (circle radius of curvature given by the mode index), which is coupled out diffractively. For the Rudin–Shapiro and randomized cases, the structure is very similar, though the circles appear narrower. This narrowing is due to the fact that amplified spontaneous emission narrows the spectrum, reducing the spectral blurring of the observed bands. As the pitch is reduced compared to the  $d = 380$  nm samples, the circles do not intersect at  $\mathbf{k}_{\parallel} = 0$ , but rather, at four intersection points at approximately  $k_{\parallel}/k_0 \sim 0.4$ . For the lasing lattices, lasing occurs close to these four intersection points, and at secondary lasing spots across the entire back aperture, generated by diffraction. The output patterns now do not simply reflect the Fourier transform of the lattice, as the output is not due to diffraction of one lasing peak at  $k_{\parallel} = 0$ , but rather, is due to the diffraction of a quartet of lasing peaks.

We assign the observation of new lasing conditions to the fact that the aperiodic arrays have many more peaks in the Fourier spectrum, which give rise to new Bragg-like diffraction conditions. This can be illustrated using a calculated band diagram, as shown in Fig. 5. For a periodic system, one can find the repeated-zone-scheme free-photon dispersion by convolving the dispersion relation  $|\mathbf{k}_{\parallel}| = \omega n_{\text{WG}}/c$  with the structure factor of the lattice, i.e., the comb of  $\delta$ -peaks situated at  $(m, n)2\pi/d$  [60]. Here, the convolution is in wave vector space. Although a band structure has no formal meaning, one can arguably find an apparent repeated-zone-scheme free-photon dispersion for

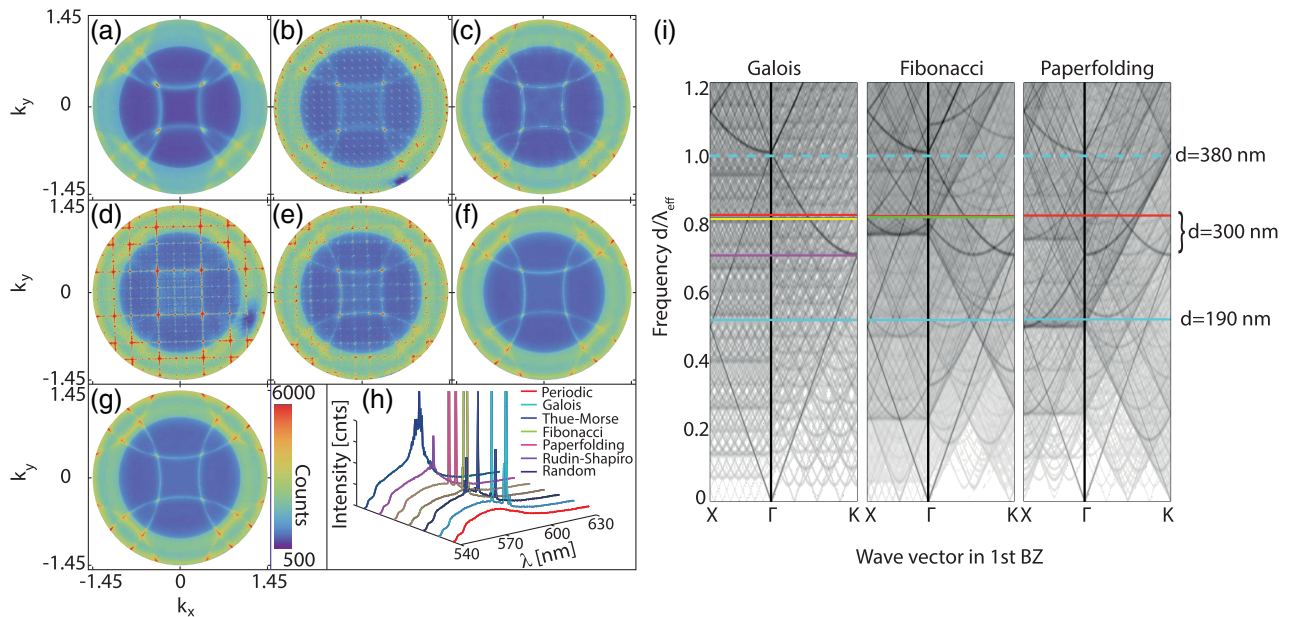


**Fig. 5.** Fourier images above lasing threshold for a pitch of 300 nm (a)–(g) and spectra for all arrays at the maximum pump power. As can be seen in panel (h), the lasing wavelength is different for each structure. The periodic system does not show a lasing peak. Panel (i): calculated band diagrams for Galois, Fibonacci, and paperfolding arrays. Horizontal colored lines represent measured lasing peak frequencies for the lattices with 380, 190, and 300 nm pitch plotted in normalized units  $n_{\text{WG}}d/\lambda$  (where  $\lambda$  is measured wavelength,  $d$  is the nominal pitch, and  $n_{\text{WG}} = 1.54$ , assumed to be fixed). Solid (dashed) cyan lines represent the  $d = 380$  nm ( $d = 190$  nm) samples, lasing at second- resp. first-order Bragg diffraction ( $n_{\text{WG}}d/\lambda$  equals 1 resp. 0.5). The other lines (around 0.7–0.85) correspond to various lasing conditions for  $d = 300$  nm.

quasi-periodic systems by convolution with the structure factors in Fig. 1. Figure 5(j) shows the results for the Fibonacci, Galois, and paperfolding lattices, which present a pure-point spectrum. Indicated as horizontal lines are normalized lasing frequencies ( $n_{\text{WG}}d/\lambda_0$ ) at which we obtain lasing in the experiments. Samples with  $d = 380$  nm lase at second-order Bragg diffraction, while at half the pitch,  $d = 190$  nm, the lasing matches the first-order Bragg diffraction. The  $d = 300$  samples lase at various conditions, notably at band crossings that occur in several of the structures at  $d/\lambda_{\text{WG}} \approx 0.8$ , and at the M-point in case of the Galois lattice. While the observed lasing conditions in these samples correlate with the “strong” crossings in the dispersion diagrams that one would expect to correspond to stop gaps amenable to lasing, actually predicting dominant lasing conditions is not easy. It is not just that the appearance of a (pseudo)-Bragg condition is required, but also that the dye gain window enters as a weighting factor.

## 7. CONCLUSION AND OUTLOOK

We have observed lasing in quasi- and aperiodic plasmonic particle arrays. Lasing occurs under the second-order Bragg diffraction condition of the underlying lattice whenever it lies in the gain window, quite independently of the spectral flatness of the structure. Above the lasing threshold, all Fourier images show that the angular distribution of laser emission inherits its shape from the Fourier transform of the lattice, consistent with diffraction of the  $k_{\parallel} = 0$  lasing mode upon outcoupling. In addition, the deterministic aperiodicity manifests itself in a speckle pattern with distinct autocorrelations. Other underlying lattice pitches result in multi-frequency lasing, where the lasing condition is related to pseudo-Bragg conditions, consistent with calculated band diagrams. These results show that periodic plasmon lasers can be beam shaped at will by removing particles, essentially imprinting the Fourier transform of the resulting binary amplitude mask on the angular output. Conversely, the correlated speckle might be useful for speckle-based imaging techniques and structured illumination microscopy. For future experiments, it would be interesting to determine if certain aperiodic lattices optimize field enhancement in order to lower lasing thresholds [26]. In our system, lasing occurs mainly by virtue of strong scattering, while plasmonic field enhancement is likely not important, since less than 1% of dye molecules are close than 10 nm to a metal particle and since we use an efficient dye. If one would use a very inefficient dye as a gain medium, one could benefit from Purcell enhancement to ensure that the gain is localized right at the plasmonic hot spots. In turn, this opens the door to study the proposed ideas that quasi-random and deterministic aperiodic structures are advantageous for engineering large area field enhancement [26,48–50]. In addition, our work paves the way to study many other quasi-periodicities in the context of lasing. For example, it has been predicted that golden-angle spirals exhibit an analogue to the band edge modes of periodic systems [29], and it would be interesting to find out if lasing can take place on these band edge modes. Penrose [42] and hyperuniform [61] lattices are other examples for which band gaps and localized states exist; these would be interesting in the context of lasing.

**Funding.** Stichting voor Fundamenteel Onderzoek der Materie (FOM); Nederlandse Organisatie voor Wetenschappelijk Onderzoek (NWO); NanoNextNL; NWO-Vici grant.

**Acknowledgment.** The authors thank Marko Kamp, Clara Osorio, and Sarah Brittan for fruitful discussions.

## REFERENCES

1. P. L. Stiles, J. A. Dieringer, N. C. Shah, and R. R. Van Duyne, “Surface-enhanced Raman spectroscopy,” *Annu. Rev. Anal. Chem.* **1**, 601–626 (2008).
2. G. Lozano, D. J. Louwers, S. R. K. Rodriguez, S. Murai, O. T. A. Jansen, M. A. Verschuuren, and J. Gómez Rivas, “Plasmonics for solid-state lighting: enhanced excitation and directional emission of highly efficient light sources,” *Light* **2**, e66 (2013).
3. J. N. Anker, W. P. Hall, O. Lyandres, N. C. Shah, J. Zhao, and R. P. Van Duyne, “Biosensing with plasmonic nanosensors,” *Nat. Mater.* **7**, 442–453 (2008).
4. M. E. Stewart, C. R. Anderton, L. B. Thompson, J. Maria, S. K. Gray, J. A. Rogers, and R. G. Nuzzo, “Nanostructured plasmonic sensors,” *Chem. Rev.* **108**, 494–521 (2008).
5. S. Mokkaapati and K. R. Catchpole, “Nanophotonic light trapping in solar cells,” *J. Appl. Phys.* **112**, 101101 (2012).
6. H. A. Atwater and A. Polman, “Plasmonics for improved photovoltaic devices,” *Nat. Mater.* **9**, 205–213 (2010).
7. M. S. Tame, K. R. McEnery, Ş. K. Özdemir, J. Lee, S. A. Maier, and M. S. Kim, “Quantum plasmonics,” *Nat. Phys.* **9**, 329–340 (2013).
8. W. L. Barnes, A. Dereux, and T. W. Ebbesen, “Surface plasmon subwavelength optics,” *Nature* **424**, 824–830 (2003).
9. L. Zhao, K. L. Kelly, and G. C. Schatz, “The extinction spectra of silver nanoparticle arrays: Influence of array structure on plasmon resonance wavelength and width,” *J. Phys. Chem. B* **107**, 7343–7350 (2003).
10. A. A. Penzkofer and Y. Lu, “Fluorescence quenching of rhodamine 6g in methanol at high concentration,” *Chem. Phys.* **103**, 399–405 (1986).
11. G. Vecchi, V. Giannini, and J. Gómez Rivas, “Shaping the fluorescent emission by lattice resonances in plasmonic crystals of nanoantennas,” *Phys. Rev. Lett.* **102**, 146807 (2009).
12. J. Stehr, J. Crewett, F. Schindler, R. Sperling, G. von Plessen, U. Lemmer, J. M. Lupton, T. A. Klar, J. Feldmann, A. W. Holleitner, M. Forster, and U. Scherf, “A low threshold polymer laser based on metallic nanoparticle gratings,” *Adv. Mater.* **15**, 1726 (2003).
13. M. J. H. Marell, B. Smalbrugge, E. J. Geluk, P. J. van Veldhoven, B. Barcones, B. Koopmans, R. Nötzel, M. K. Smit, and M. T. Hill, “Plasmonic distributed feedback lasers at telecommunications wavelengths,” *Opt. Express* **19**, 15109–15118 (2011).
14. J. Y. Suh, C. H. Kim, W. Zhou, M. D. Huntington, D. T. Co, M. R. Wasielewski, and T. W. Odom, “Plasmonic bowtie nanolaser arrays,” *Nano Lett.* **12**, 5769–5774 (2012).
15. W. Zhou, M. Dridi, J. Y. Suh, C. H. Kim, D. T. Co, M. R. Wasielewski, G. C. Schatz, and T. W. Odom, “Lasing action in strongly coupled plasmonic nanocavity arrays,” *Nat. Nanotechnol.* **8**, 506–511 (2013).
16. A. H. Schokker and A. F. Koenderink, “Lasing at the band edges of plasmonic lattices,” *Phys. Rev. B* **90**, 155452 (2014).
17. A. Yang, T. B. Hoang, M. Dridi, C. Deeb, M. H. Mikkelsen, G. C. Schatz, and T. W. Odom, “Real-time tunable lasing from plasmonic nanocavity arrays,” *Nat. Commun.* **6**, 6939 (2015).
18. D. S. Wiersma, M. P. van Albada, and A. Lagendijk, “Random laser,” *Nature* **373**, 203–204 (1995).
19. D. Wiersma and A. Lagendijk, “Light diffusion with gain and random lasers,” *Phys. Rev. E* **54**, 4256–4265 (1996).
20. H. Cao, Y. Zhao, S. Ho, E. Seelig, Q. Wang, and R. Chang, “Random laser action in semiconductor powder,” *Phys. Rev. Lett.* **82**, 2278–2281 (1999).
21. D. S. Wiersma, “The physics and applications of random lasers,” *Nat. Phys.* **4**, 359–367 (2008).
22. E. Maciá, “Exploiting aperiodic designs in nanophotonic devices,” *Rep. Prog. Phys.* **75**, 036502 (2012).
23. A. Gopinath, S. V. Boriskina, N.-N. Feng, B. M. Reinhard, and L. Dal Negro, “Photonic-plasmonic scattering resonances in deterministic aperiodic structures,” *Nano Lett.* **8**, 2423–2431 (2008).
24. C. Forestiere, G. F. Walsh, G. Miano, and L. Dal Negro, “Nanoplasmonics of prime number arrays,” *Opt. Express* **17**, 24288–24303 (2009).
25. M. Florescu, S. Torquato, and P. J. Steinhardt, “Complete band gaps in two-dimensional photonic quasicrystals,” *Phys. Rev. B* **80**, 155112 (2009).

26. L. Dal Negro and S. V. Boriskina, "Deterministic aperiodic nanostructures for photonics and plasmonics applications," *Laser Photon. Rev.* **6**, 178–218 (2012).
27. S. V. Boriskina and L. Dal Negro, "Sensitive label-free biosensing using critical modes in aperiodic photonic structures," *Opt. Express* **16**, 12511–12522 (2008).
28. S. V. Boriskina, A. Gopinath, and L. Dal Negro, "Optical gaps, mode patterns and dipole radiation in two-dimensional aperiodic photonic structures," *Phys. Rev. E* **41**, 1102–1106 (2009).
29. L. Dal Negro, *Optics of aperiodic structures* (Pan Stanford, 2014).
30. Z. V. Vardeny, A. Nahata, and A. Agrawal, "Optics of photonic quasicrystals," *Nat. Photonics* **7**, 177–187 (2013).
31. E. Maciá, "The role of aperiodic order in science and technology," *Rep. Prog. Phys.* **69**, 397–441 (2006).
32. D. Levine and P. J. Steinhardt, "Quasicrystals. I. Definition and structure," *Phys. Rev. B* **34**, 596–616 (1986).
33. D. Shechtman, I. Blech, D. Gratias, and J. W. Cahn, "Metallic phase with long range orientational order and no translation symmetry," *Phys. Rev. Lett.* **53**, 1951–1953 (1984).
34. B. le Feber, J. Cesario, H. Zeijlemaker, N. Rotenberg, and L. Kuipers, "Exploiting long-ranged order in quasiperiodic structures for broadband plasmonic excitation," *Appl. Phys. Lett.* **98**, 201108 (2011).
35. M. Ghulinyan, C. Oton, L. Dal Negro, L. Pavesi, R. Sapienza, M. Colocci, and D. Wiersma, "Light-pulse propagation in Fibonacci quasicrystals," *Phys. Rev. B* **71**, 094204 (2005).
36. M. Stockman, "Inhomogeneous eigenmode localization, chaos, and correlations in large disordered clusters," *Phys. Rev. E* **56**, 6494–6507 (1997).
37. C.-W. Lee, G. Singh, and Q. Wang, "Light extraction—a practical consideration for a plasmonic nano-ring laser," *Nanoscale* **5**, 10835–10838 (2013).
38. S. Y. Lee, J. J. Amsden, S. V. Boriskina, A. Gopinath, A. Mitropoulos, D. L. Kaplan, F. G. Omenetto, and L. Dal Negro, "Spatial and spectral detection of protein monolayers with deterministic aperiodic arrays of metal nanoparticles," *Proc. Natl. Acad. Sci. USA* **107**, 12086–12090 (2010).
39. J. H. Lin, W. L. Chang, H.-Y. Lin, T.-H. Chou, H.-C. Kan, and C. C. Hsu, "Enhancing light extraction efficiency of polymer light-emitting diodes with a 12-fold photonic quasi crystal," *Opt. Express* **21**, 22090–22097 (2013).
40. L. Dal Negro, N.-N. Feng, and A. Gopinath, "Electromagnetic coupling and plasmon localization in deterministic aperiodic arrays," *J. Opt. A* **10**, 064013 (2008).
41. A. Lagendijk, B. van Tiggelen, and D. Wiersma, "Fifty years of Anderson localization," *Phys. Today* **62**(8), 24–29 (2009).
42. M. Notomi, H. Suzuki, T. Tamamura, and K. Edagawa, "Lasing action due to the two-dimensional quasiperiodicity of photonic quasicrystals with a Penrose lattice," *Phys. Rev. Lett.* **92**, 123906 (2004).
43. J.-K. Yang, S. V. Boriskina, H. Noh, M. J. Rooks, G. S. Solomon, L. Dal Negro, and H. Cao, "Demonstration of laser action in a pseudorandom medium," *Appl. Phys. Lett.* **97**, 223101 (2010).
44. L. Mahler, A. Tredicucci, F. Beltram, C. Walther, J. Faist, H. E. Beere, D. A. Ritchie, and D. S. Wiersma, "Quasi-periodic distributed feedback laser," *Nat. Photonics* **4**, 165–169 (2010).
45. D. Luo, Q. G. Du, H. T. Dai, H. V. Demir, H. Z. Yang, W. Ji, and X. W. Sun, "Strongly linearly polarized low threshold lasing of all organic photonic quasicrystals," *Sci. Rep.* **2**, 627 (2012).
46. A. H. Schokker and A. F. Koenderink, "Statistics of randomized plasmonic lattice lasers," *ACS Photon.* **2**, 1289–1297 (2015).
47. A. Barbe and F. Von Haeseler, "Correlation and spectral properties of multidimensional Thue–Morse sequences," *Int. J. Bifurcation Chaos* **17**, 1265–1303 (2007).
48. Y. Nishijima, L. Rosa, and S. Juodkakis, "Surface plasmon resonances in periodic and random patterns of gold nano-disks for broadband light harvesting," *Opt. Express* **20**, 11466–11477 (2012).
49. Y. Nishijima, J. B. Khurgin, L. Rosa, H. Fujiwara, and S. Juodkakis, "Randomization of gold nano-brick arrays: a tool for SERS enhancement," *Opt. Express* **21**, 13502–13514 (2013).
50. Y. Nishijima, J. B. Khurgin, L. Rosa, H. Fujiwara, and S. Juodkakis, "Tunable Raman selectivity via randomization of a rectangular pattern of nanodisks," *ACS Photon.* **1**, 1006–1012 (2014).
51. I. Sersic, C. Tuambilangana, and A. F. Koenderink, "Fourier microscopy of single plasmonic scatterers," *New J. Phys.* **13**, 083019 (2011).
52. N. Meinzer, W. L. Barnes, and I. R. Hooper, "Plasmonic meta-atoms and metasurfaces," *Nat. Photonics* **8**, 889–898 (2014).
53. G. van Soest, F. J. Poelwijk, and A. Lagendijk, "Speckle experiments in random lasers," *Phys. Rev. E* **65**, 046603 (2002).
54. H. Yilmaz, E. G. van Putten, J. Bertolotti, A. Lagendijk, W. L. Vos, and A. P. Mosk, "Speckle correlation resolution enhancement of wide-field fluorescence imaging," *Optica* **2**, 424–429 (2015).
55. E. Mudry, K. Belkebir, J. Girard, J. Savatier, E. Le Moal, C. Nicoletti, M. Allain, and A. Sentenac, "Structured illumination microscopy using unknown speckle patterns," *Nat. Photonics* **6**, 312–315 (2012).
56. O. Katz, P. Heidmann, M. Fink, and S. Gigan, "Non-invasive single-shot imaging through scattering layers and around corners via speckle correlations," *Nat. Photonics* **8**, 784–790 (2014).
57. E. T. F. Rogers, J. Lindberg, T. Roy, S. Savo, J. E. Chad, M. R. Dennis, and N. I. Zheludev, "A super-oscillatory lens optical microscope for sub-wavelength imaging," *Nat. Mater.* **11**, 432–435 (2012).
58. M. G. L. Gustafsson, L. Shao, P. M. Carlton, C. J. R. Wang, I. N. Golubovskaya, W. Z. Cande, D. A. Agard, and J. W. Sedat, "Three-dimensional resolution doubling in wide-field fluorescence microscopy by structured illumination," *Biophys. J.* **94**, 4957–4970 (2008).
59. A. Sentenac, P. C. Chaumet, and K. Belkebir, "Beyond the Rayleigh criterion: grating assisted far-field optical diffraction tomography," *Phys. Rev. Lett.* **97**, 243901 (2006).
60. L. Langguth, A. H. Schokker, K. Guo, and A. F. Koenderink, "Plasmonic phase-gradient metasurface for spontaneous emission control," *Phys. Rev. B* **92**, 205401 (2015).
61. W. Man, M. Florescu, K. Matsuyama, P. Yadak, G. Nahal, E. Hashemizad, S. Williamson, P. Steinhardt, S. Torquato, and P. Chaikin, "Photonic band gap in isotropic hyperuniform disordered solids with low dielectric contrast," *Opt. Express* **21**, 19972–19981 (2013).